



Subglacial discharge effects on basal melting of a rotating, idealized ice shelf

Irena Vaňková¹, Xylar Asay-Davis¹, Carolyn Branecky Begeman¹, Darin Comeau¹, Alexander Hager¹, Matthew Hoffman¹, Stephen F. Price¹, and Jonathan Wolfe¹

¹Los Alamos National Laboratory, Los Alamos, NM 87545, USA

Correspondence: Irena Vaňková (vankova@lanl.gov)

Abstract. When subglacial meltwater is discharged into the ocean at the grounding line, it acts as a source of buoyancy, enhancing flow speeds along the ice base that result in higher basal melt rates. The effects of subglacial discharge have been well studied in the context of a Greenland-like, vertical calving front, where Earth's rotation can be neglected. Here we study these effects in the context of Antarctic ice shelves, where rotation is important. We use a numerical model to simulate ocean circulation and basal melting beneath an idealized three-dimensional ice shelf and vary the rate and distribution of subglacial discharge. For channelized discharge, we find that in the rotating case melt rate increases with two-thirds power of the discharge, in contrast with existing non-rotating results for which the melt rate increases with one-third power of the discharge. For distributed discharge, we find that in both rotating and non-rotating cases melt rate increases with two-thirds power of the discharge. Furthermore, in the rotating case, the addition of channelized subglacial discharge can produce either higher or lower ice-shelf basal melt-rate increase than the equivalent amount of distributed discharge, depending on its location along the grounding line relative to the directionality of the Coriolis force. This contrasts with previous results from non-rotating, vertical ice-cliff simulations, where distributed discharge was always found to be more efficient at enhancing terminus-averaged melt rate than channelized discharge. The implication, based on our idealized simulations, is that melt-rate parameterizations attempting to include subglacial discharge effects that are not geometry and rotation aware may produce spatially averaged melt rates that are off by a factor of two or more.

1 Introduction

Subglacial freshwater originates as meltwater formed at the glacier bed, or as meltwater draining there from supraglacial or englacial sources. It is discharged into the ocean at the grounding line, where the ice goes afloat. Being released at depth, this freshwater is a source of buoyancy that accelerates as an ascending meltwater plume along the ice-shelf base or the vertical calving face, enhancing entrainment of ambient waters, and modulating melt rates. In Alaska and Greenland, where supraglacial melting is a significant contributor to subglacial discharge, local measurements near marine-terminating glaciers have shown such high seasonal submarine melting that it could only have been driven by enhanced subglacial discharge from summer surface melt (Motyka et al., 2003; Washam et al., 2019). Circulation and renewal in some fjords has been shown to be driven almost entirely by subglacial discharge (Gladish et al., 2015; Carroll et al., 2017; Slater et al., 2018; Hager et al.,



25 2022b). Meanwhile, the importance of subglacial discharge on sub-ice shelf circulation and melting in Antarctica is less clear, because the drainage of supraglacial meltwater to the bed is lacking, and present-day subglacial discharge is sourced only from much smaller magnitude subglacial melting. However, there has been recent surge of interest in the influence of subglacial discharge on basal melting beneath Antarctic ice shelves. Dow et al. (2022) and Hager et al. (2022a) demonstrate that the large catchment sizes in some parts of Antarctica, when combined with high subglacial melting, can lead to subglacial discharge
30 fluxes similar in magnitude to the surface-derived melt fluxes in Greenland. Dow et al. (2022) found correspondence between elevated satellite-derived basal melt rates near grounding lines and locations of modeled subglacial meltwater discharge at some ice shelves. Pelle et al. (2023) found that it was necessary to incorporate a parameterization of subglacial discharge effects (Jenkins, 2011) on basal melting with plume theory (Jenkins, 1991; Lazeroms et al., 2018) to achieve reasonable agreement with satellite-derived basal melt rates, as two-dimensional plume theory on its own underestimated localized high
35 melting near an inferred subglacial channel.

While several studies have implemented subglacial discharge into Antarctic regional domains and studied its effects on circulation beneath ice shelves, basal melting, and continental shelf properties (Nakayama et al., 2021; Goldberg et al., 2023; Gwyther et al., 2023), the current understanding of melt-rate sensitivities to subglacial discharge is, with exception of the work of Wekerle et al. (2024), primarily based on plume theory (Jenkins, 2011) and on idealized studies focused on a Greenland-
40 like, vertical ice front (Xu et al., 2012, 2013; Kimura et al., 2014; Slater et al., 2015) or a narrow ice tongue (Cai et al., 2017; Wiskandt et al., 2023). Jenkins (2011) included subglacial discharge in non-rotational, one-dimensional plume theory. Using dimensional analysis he found that melt rate, within some distance from the freshwater source, has a linear dependence on temperature, and one-third power dependence on subglacial discharge. These theoretical results were to some extent reproduced in non-rotational idealized numerical simulations of melting, two-dimensional vertical faces (Xu et al., 2012; Sciascia et al.,
45 2013), two-dimensional ice tongues (Cai et al., 2017; Wiskandt et al., 2023), and three-dimensional vertical faces (Xu et al., 2013; Kimura et al., 2014). These studies typically find a sub-linear, power-law relationship between melt rates (\dot{m}) and subglacial discharge (F_s) of the form $\dot{m} \sim F_s^n$ with $n < 1$. While Xu et al. (2012) found $n = \frac{1}{3}$, in line with theory, the remaining idealized, two-dimensional studies found slightly stronger melt-rate dependence on subglacial discharge; Sciascia et al. (2013) found $n = 0.5$, Cai et al. (2017) found $n = 0.57$, and Wiskandt et al. (2023) found n between 0.41 and 0.47 for
50 different fjord temperatures. The three-dimensional study of Xu et al. (2013) also found stronger melt-rate dependence on subglacial discharge, with n between 0.5-0.9, as opposed to the theoretical one-third power. Kimura et al. (2014) found a more complex functional relationship with melt rate saturating once a critical discharge rate has been reached and the resulting high inflow velocity forced the plume away from the ice face. Wekerle et al. (2024) found $n = \frac{1}{2}$ in a three-dimensional, global realistic configuration focused the 79 North Glacier Tongue that included rotation. However, in their study shelf conditions
55 could evolve as a function of discharge given their configuration was global and shelf conditions were not restored, allowing for conflation of the discharge and shelf temperatures effects on melting. Finally, Jackson et al. (2022) addressed the relationship between basal melting and discharge observationally. Their estimates from a relatively warm, Alaskan glacier showed that plume theory underestimated melting by over an order of magnitude, but the one-third power dependence of melt rate on discharge seemed to hold, although with substantial uncertainties.



60 The question of how the horizontal distribution of subglacial discharge along grounding lines affects melt rates has also been addressed before to some extent. Kimura et al. (2014) considered the case for an unstratified water column and found that two channels in close proximity produced higher melt rates than a single channel with the equivalent total discharge. Slater et al. (2015) considered a more realistic, stratified setup, in which plumes can reach neutral buoyancy, and found that distributed discharge always produces higher total melt rate than the equivalent channelized discharge.

65 Crucially, what the convectively forced plume model and the existing idealized numerical studies have neglected is the effect of the Earth's rotation, as have all other common basal melt-rate parameterizations used to force ice-sheet models (Burgard et al., 2022), including those that incorporate subglacial discharge (Pelle et al., 2023). While the omission of Earth's rotation is appropriate in some of these studies that focus on vertical ice cliffs, it is not appropriate for Antarctic-like, ice-shelf cavities. In this paper, we revisit the relationship between submarine melting and subglacial discharge for a rotating, Antarctic-like
70 configuration. The simulations are idealized and their purpose is to provide insight into melt-rate sensitivities to subglacial discharge that, in a realistic global configuration, would be computationally expensive and potentially challenging to interpret. The idealized simulations are performed using relatively coarse resolution compared to the Greenland-like, vertical ice-cliff studies, in line with the goal of understanding sensitivities in realistic, global model configurations.

2 Methods

75 For idealized testing, we use the ocean component of the Energy Exascale Earth System Model (E3SM), the Model for Prediction Across Scales-Ocean (MPAS-Ocean; Ringler et al., 2013). MPAS-Ocean is a finite-volume, ocean model that solves the hydrostatic Boussinesq equations. It uses a horizontal mesh defined by a centroidal Voronoi tessellation. The simulations presented here use a planar mesh, rather than one on the surface of a sphere. Our experimental setup follows the Ocean0 configuration (Figure 1) from the second Ice Shelf-Ocean Model Intercomparison Project, ISOMIP+ (Asay-Davis et al., 2016).
80 We use the z^* vertical coordinate (Adcroft and Campin, 2004) in the open ocean. Beneath ice shelves the coordinate follows the ice draft and at the seafloor layers are dropped when they intersect the bathymetry. The Ocean0 experiments presented here are performed with 36 vertical levels and 2-km horizontal resolution. Sensitivity runs with 1-km and 4-km resolutions were also run and produced qualitatively similar results. We note that the change in resolution can be largely compensated for through an appropriate change in horizontal viscosity. We use the linear equation of state. The ice-shelf geometry is static and
85 ice-shelf basal melting is calculated using the three-equation parameterization with standard coefficients (Holland and Jenkins, 1999). Following Losch (2008), temperature and salinity for calculating thermal driving for ice-shelf basal melting are found by vertically-averaging over cells within 10 m of the ice base. Heat and freshwater fluxes associated with basal melting are distributed into the ocean based on an exponential profile, with a decay length scale of 10 m. Frazil ice is allowed to form, but it is not advected with the flow. At each time step, the model checks for frazil ice formation in the top 100 m of the water
90 column, and any frazil mass is brought to the surface immediately and added to interfacial basal melting. The rotating cases use an f plane configuration with the Coriolis parameter of $f = -1.409 \cdot 10^{-4} \text{ s}^{-1}$, which corresponds to the latitude of 75° South.



Initially, potential temperature and salinity are prescribed as horizontally uniform and linearly increasing with depth, with surface values of $T_s = -1.9^\circ\text{C}$ and $S_s = 33.8$ PSU in all cases. In the base case, the properties at the deepest point are $T_b = 1^\circ\text{C}$ and $S_b = 34.7$ PSU. At the northern boundary, potential temperature and salinity are restored to the initial values throughout the simulations. No slip boundary conditions are applied at the side walls. Subglacial discharge into the ocean at the grounding line is implemented as a volume flux of freshwater at the local pressure-dependent freezing point. Because there is no prescribed evaporation, sea level in the idealized domain increases over time due to the flux of subglacial discharge and ice-shelf basal melt into the domain. The circulation within the ice-shelf cavity is entirely driven by buoyancy forcing from ice-shelf basal melt and grounding-line freshwater flux. The simulations were run for two years, by which time the melt-rate pattern developed and stabilized. Analysis is based on the last monthly mean outputs from the two-year simulations.

In the first set of experiments we study melt-rate response to varying F_s , the spatially integrated subglacial freshwater flux, and how this response changes with different F_s distributions along the grounding line in a rotating framework. We prescribe the boundary shelf conditions as in the base case ($T_b = 1^\circ\text{C}$ and $S_b = 34.7$ PSU). We then vary total F_s between 0 and $720 \text{ m}^3 \text{ s}^{-1}$. For each tested F_s value, we also vary its horizontal release location (Figure 1e) as follows:

- (L) F_s is distributed along a line corresponding to the deepest part of the grounding line
- (PW) F_s is applied at a point, in the western most grid cell of L (in the case described immediately above)
- (PC) F_s is applied at a point, in the center grid cell of L
- (PE) F_s is applied at a point, in the eastern most grid cell of L

This set of experiments was also carried out in a non-rotating framework, setting $f = 0$, for comparison of our findings with those from previous studies.

The next set of experiments tests melt-rate sensitivity to varying amount of F_s across different potential temperatures. We keep the surface temperature fixed at -1.9°C , and vary the sea floor potential temperature T_b between -1.9°C and 4°C . The temperature profile was kept linear, and salinity was adjusted to keep the same density profile in all simulations. This sensitivity test was performed for a distributed discharge (L) in a rotating framework.

By design, some models, such as MPAS-Ocean, are required to have more than a single layer at the grounding line. This then brings up the modeling choice of where to apply F_s in the vertical. In the above experiments we chose to distribute F_s uniformly in the vertical. To test melt-rate sensitivity to this modeling choice we varied the vertical distribution of F_s as follows:

- (T) F_s is concentrated in the top vertical layer
- (U) F_s is uniformly mixed in the vertical
- (B) F_s is concentrated in the bottom vertical layer

This sensitivity test was performed for a distributed discharge in a rotating framework for three different bottom potential temperatures, -1°C , 0°C , and 1°C .



125 3 Results

With $F_s = 0$, the spatially averaged melt rate over the ice shelf increases quadratically with the far-field potential temperature (Figure 2a), in agreement with previous simulations (Holland et al., 2008) and theory (Jenkins et al., 2018). Melt rates are proportional to friction velocity and thermal driving. In the rotating case, the melt-rate spatial pattern is such that melting is highest at the deepest parts of the ice shelf and enhanced at the western grounding line (Figure 3a1). This holds as long as the thermal driving remains sufficient (Figure 3a3) to support melting, while the ascending meltwater plume veers westward under the influence of Coriolis force (Figure 3a2). Friction velocity shown here in figures (e.g., Figure 3, second column) is a good proxy for plume speed as long as the plume is attached to the ice base.

The interplay between friction velocity and thermal driving, when F_s is introduced, is shown in Figure 3 for the rotating case and in Figure 4 for the non-rotating one. F_s enhances friction velocities (e.g., Figure 3e2 and Figure 4e2) due to added buoyancy, increasing melt that cools the boundary layer (e.g., Figure 3e3 and Figure 4e3), which in turn suppresses melt. Near the F_s source, the friction velocity increase is so high that it dominates any cooling, producing positive melt-rate anomalies; however with increasing distance from the source, melt-driven cooling starts compensating the heightened friction velocity, resulting in little change in melt rates (e.g., Figure 3e1 and Figure 4e1). The plume slows down quickly as it rises, entrains ambient waters, and thickens. In the rotating case, the plume veers westward relative to its direct, upslope and northward direction with no rotation. The result is meltwater accumulation near the western grounding line (Figure 5a2), compared to the east (Figure 5a1), and increased overall stratification with lighter waters at the surface and meltwater extending deeper into the water column in the west (Figure 5a2). This asymmetry, present already in the reference case, sets the stage for the observed differences in melt response when F_s is introduced and its release location is varied along the grounding line.

When evaluating simulations with F_s , the primary quantity of interest is $\Delta\dot{m}$, the anomaly in spatially averaged basal melt rates with respect to the reference case with $F_s = 0$. As the analysis is focused on the last monthly mean output (of 24 months of simulation) $\Delta\dot{m}$ is also averaged in time. We observe that the functional form of the sub-linear relationship between $\Delta\dot{m}$ and F_s appears to differ depending on whether rotation is included and whether F_s is distributed or channelized (Figure 6a-b). We also observe substantial sensitivity of $\Delta\dot{m}$ to the horizontal F_s release location (Figure 6a) that is qualitatively different between the rotating and non-rotating cases. These observations are investigated next.

Unless stated otherwise, the sections and spatial patterns shown and discussed in figures 3, 7, 4, 8, and 5 are for the moderate discharge strength of $F_s = 72 \text{ m}^3/\text{s}$. The results do not change qualitatively with the strength of F_s within the tested range of values.

3.1 Melt-rate sensitivity to horizontal discharge release location

Starting with the rotating case, the point-source experiments (PW, PC, and PE) show that the most effective location to apply F_s in terms of $\Delta\dot{m}$ is at the eastern portion of the grounding line; $\Delta\dot{m}$ more than doubles when F_s is applied in the east, rather than in the west (Figure 6a). When an equivalent F_s is distributed along the grounding line (L), the resulting $\Delta\dot{m}$ is approximately halfway between the $\Delta\dot{m}$ in the PW and PE cases, and is slightly higher than in the PC case. $\Delta\dot{m}$ in the PE case



is about 1.5 times higher than in the distributed (L) case. This is in part due to a larger portion of the ice-shelf area sustaining positive melt-rate anomalies when the plume is located farther east on the grounding line (Figure 3e1) compared to its central (Figure 3d1) or western location (Figure 3c1). Consistent with the point-source experiment, the distributed case experiences a larger spatial extent of melt-rate increase in the east than in the west (Figure 3b1).

When F_s is released at a point in the east (PE), where the water column is less stratified (Figure 5c1), the added freshwater induces high flow speeds, cooling, and freshening in a narrow layer near the ice base, with relative warming beneath it (Figure 7e1). This pattern persists as the plume rises, spreads, and turns west (Figure 7e2). However, along the eastern and central transects no portion of the plume has reached neutral buoyancy as it does in the non-rotating case (Figure 8e1). Instead, the plume becomes neutral buoyant in the western part of the domain, where the presence of the western boundary forces the plume to flow upslope, rise and mix, as visible in the large temperature anomaly throughout the western section (Figure 7e3). The addition of F_s has increased vertical mixing in the west, as evidenced by relative warming at the top and relative cooling at the bottom of the water column.

When F_s is released at a point in the center of the grounding line (PC), the response downstream of the release location is similar to the PE case, only weaker (Figure 7d vs Figure 7e). The friction velocity increase is lower in this case (Figure 3d2 vs Figure 3e2) because the water column is more stratified here, having already been freshened by meltwater coming from the east. This also means, that the density difference between the subglacial discharge and the surface waters is reduced, as is the driving force for the plume ascent. Finally, the presence of the western boundary means that, the closer the discharge location is to the west, the less distance the plume is able to travel across the ice shelf before it encounters the boundary and is forced upward along the ice base (Figure 3, second column).

When F_s is released at a point near the western boundary (PW), these tendencies are even more amplified. The water column is more stratified here, the surface water along the ice base fresher and lighter (Figure 5b2), and the proximity of the western boundary closer, which forces upward flow of meltwater almost immediately upon release (Figure 3). The result is that the plume has less distance to travel along the ice base and it becomes neutrally buoyant deeper in the water column. This is seen as relative warming at the top and relative cooling at the bottom of the water column, much closer to the grounding line (Figure 7c3). Unlike in the PE and PC cases, for PW this relative warming at the top extends as far as the boundary layer, causing a warm anomaly in the thermal driving (Figure 3c3).

In summary, the east-west asymmetry in meltwater distribution means that F_s added in the west inputs less buoyancy, and therefore less available potential energy into the system than F_s added in the east. Together with the east-west asymmetry in stratification, this means that when injected in the west the plume becomes neutrally buoyant deeper in the water column, keeping any positive melt-rate anomalies closer to the grounding line and lowering their magnitude (Figure 3, left column).

3.2 Relationship between subglacial discharge and melt

We now investigate how the functional form of the sub-linear relationship between F_s and $\Delta\dot{m}$ depends on rotation and on the channelization of the drainage system. We first remove differences associated with the domain asymmetries and the presence of boundaries by averaging the $\Delta\dot{m}$ results for all three point release cases separately for the rotating and the non-rotating



scenarios (Figure 6a-b). We confirm that the non-rotating case complies with theory, that is, $\Delta\dot{m}$ scales with one-third power of F_s , as in Jenkins (2011) (Figure 9a, dashed blue line). However, in the rotating case, the one-third power scaling clearly overestimates $\Delta\dot{m}$ for low F_s and underestimates it for high F_s (Figure 9a, dashed red line), which means that the curvature of the one-third power scaling is incorrect. A higher power scaling seems to be a better fit for the rotating case; we find that $\Delta\dot{m}$ scales well with two-thirds power of F_s . Nevertheless, the theory of Jenkins (2011) should still hold in the rotating case at small distances from the source before the Coriolis effect becomes important. To test this, instead of averaging over the entire domain, we average melt-rate anomalies over a fixed distance from the F_s source. We compare melt-rate anomalies averaged over the whole domain, over an area within 10 km from the source, and within 2 km from the source (Figure 9a-c). We observe that, for the rotating case, the scaling between integrated melt-rate anomaly and F_s becomes closer to one-third power as melt rates are averaged over a smaller area nearer to the source (Figure 9c), as expected from the non-rotating, convectively forced plume theory. Thus, in the rotating case, the effects giving rise to the higher power in the scaling of the melt-rate anomaly with F_s are entirely non-local. We note that for the PC case alone, which, unlike the PE and PW cases, is far from the side boundaries, the scaling between integrated melt-rate anomaly and F_s becomes close to two-thirds power when the averaging takes places over an area within ~ 10 km from the source. This indicates that the higher power scaling is independent of the presence of side walls.

Turning to the distributed system, we observe that $\Delta\dot{m}$ scales with two-thirds power of F_s for both the rotating and the non-rotating case (Figure 9d, solid lines). As in the channelized case, we investigate how this scaling changes when melt-rate anomaly is averaged closer to the source. As we average only over cells within 2-km of the source, that is one grid cell distance away, the melt-rate anomaly scaling with F_s lies between one-third and two-thirds power for the non-rotating case and closer to one-third power in the rotating case (Figure 9f). However, when averaged over 10-km distance from the F_s source, the scaling is already much closer to two-thirds power for both the rotating and the non-rotating case (Figure 9e).

To check whether the scaling holds across different ambient temperatures, we run temperature sensitivity experiments for the rotating, distributed case. We find that the two-thirds power scaling holds across different values of far-field bottom potential temperature (Figure 2b), especially for interfacial melting. At colder temperatures ($T_b = -1.9^\circ\text{C}$), when significant amount of frazil forms and frazil freezing anomalies largely compensate interfacial melting anomalies, the melt-rate sensitivity to F_s drops and saturates (Figure 2b, black dashed line). Unfortunately, the representation of frazil dynamics in MPAS-Ocean is rather simplistic, so we are not in a position to investigate frazil-related dynamics in greater detail. Finally, based on the rotating, distributed case, we confirm that $\Delta\dot{m}$ depends approximately linearly on ambient potential temperature (Figure 2c) in the same way as it does in the non-rotating, convectively-forced plume theory (Jenkins, 2011). The functional fit used to produce the solid curves in Figure 2b-c is

$$\Delta\dot{m} = k(T_b - T_0)F_s^n. \quad (1)$$

We imposed $n = \frac{2}{3}$, and the remaining coefficients were obtained using a least squares fit, yielding $k = 1.89 \cdot 10^{5^\circ} \text{C}^{-1} \text{m}^{-1} \text{s}^{-1/3}$, and $T_0 = -2.67^\circ\text{C}$. T_0 is a bit lower than the freezing point, and therefore the equation does not apply well when ambient tem-



225 peratures are close to the freezing point and when frazil dynamics becomes important (Figure 2b, black dashed line), as already discussed.

4 Discussion

From our idealized experiments that include rotation, we found that channelized discharge can either increase or decrease the integrated melt-rate anomaly compared to the distributed system, in our particular setup by about 50% (Figure 6a). This contrasts with findings from non-rotating experiments by Slater et al. (2015). They modeled a Greenland-like vertical ice front and varied the distribution of freshwater discharge along the grounding line, concluding that distributed F_s is always more efficient in driving melting than channelized F_s , in their simulations by up to a factor of five. Results from our non-rotating experiments are qualitatively consistent with Slater et al. (2015), and we observe a larger $\Delta\dot{m}$ increase for horizontally distributed than for channelized discharge. This is particularly pronounced as F_s increases, owing to the higher exponent in the power-law relationship between $\Delta\dot{m}$ and F_s in the distributed case than in the channelized case (Figure 6b). A key reason the findings of Slater et al. (2015) – that melt-rate response to discharge increases with the number of sources – do not apply in the rotating case is that they rely on individual plumes not interacting with each other. In the non-rotating case, individual plumes only interact when spaced sufficiently close together, but in the rotating case the plumes interact even if spaced far from each other. Rotation eventually makes all melt from individual plumes coalesce on one side of the domain, which results in less ice-shelf area available for discharge-driven melt-rate increase compared to the non-rotating case.

The reason for the two-thirds power dependence of melt rate on F_s in the non-rotating, distributed case compared to the one-third power dependence in the channelized, non-rotating case is not clear. Although this difference has not been explicitly discussed in previous studies, it may be implicitly present in the work of Xu et al. (2013). They studied the relationship between submarine melt rate and discharge through three-dimensional simulations of a vertical ice front, finding a more complicated, sub-linear relationship than a simple power law, and identified two regimes, one appropriate for low F_s and the other for high F_s . In the light of our results, this difference can be attributed to the way variations in F_s magnitude were prescribed in their study; Xu et al. (2013) fixed the value of F_s in each grid cell and, to increase total discharge, they increased the number of grid cells where this fixed F_s was applied. Thus, for lower values of F_s , they effectively simulated a channelized system and, for higher values of F_s , the system effectively became distributed. As such, according to our results, the power law gradually changes from a one-third to a two-thirds power dependence, giving rise to the more complicated functional relationship reported on in Xu et al. (2013). Notably, the parameterization of Xu et al. (2013), subsequently adopted by the Ice Sheet Model Intercomparison Project for CMIP6 - Greenland Ice Sheet (ISMIP6-GIS; Slater et al., 2020), is widely used in ice-sheet models as the standard vertical ice-cliff melt-rate parameterization. While we are not able to simulate vertical cliffs, our results from non-rotating ice-shelf simulations suggest the functional form of the melt-rate dependence on discharge from Xu et al. (2013) to be revised. Specifically, rather than the exponent (n) being a function of the discharge strength, our simulations indicate that n depends on whether the discharge is distributed ($n = \frac{2}{3}$), or channelized ($n = \frac{1}{3}$).



Our results have implications for melt-rate parameterizations that attempt to realistically account for the effects of subglacial discharge on ice-shelf basal melting. The same amount of total discharge can more than double $\Delta\dot{m}$ if located in the east as opposed to the west of the domain (for the Southern Hemisphere). This result is based on a highly idealized ice-shelf domain, and will likely change quantitatively as additional geometric complexities are included. The sensitivity of $\Delta\dot{m}$ to discharge location along the grounding line is not accounted for in existing parameterizations (Jenkins, 2011; Pelle et al., 2023), and may be difficult to include accurately, especially for more complicated geometries. Our results highlight the sensitivity of melt rates to the location of channelized, submarine discharge and, as such, also highlight the importance of accurate modeling of subglacial meltwater discharge via subglacial hydrology models.

We have primarily focused on characterizing spatially averaged melt rates and their anomalies in the presence of subglacial discharge, as have previous ocean modeling studies of melting vertical cliffs and floating ice tongues. While some ice-sheet modeling studies indicate that spatially averaged melt rates are far more important for determining ice-sheet dynamics than their spatial variations (Joughin et al., 2024), a more extensive body of literature argues that melt rates near grounding lines and pinning points matter to the ice-sheet dynamics much more than melt rates elsewhere on the ice shelf (Gagliardini et al., 2010; Fürst et al., 2016; Reese et al., 2018; Zhang et al., 2020). An understanding of how the melt-rate anomalies due to subglacial discharge ultimately affect ice-sheet dynamics will require an ice-sheet model with a suitable melt-rate parameterization (e.g., Pelle et al., 2023) or a coupled ice-sheet/ocean/subglacial hydrology model.

5 Conclusions

We studied the effect of subglacial discharge on submarine melt rates for an idealized, Antarctic-like ice shelf within a rotating reference frame. This work complements existing studies focusing on non-rotating, idealized, Greenland-like vertical calving fronts and narrow ice tongues. The motivation for the study was to develop a conceptual understanding of the sensitivities and response of the system in an idealized setup before conducting global, realistic simulations. Relevant to the realistic simulations, we found that with restoring shelf conditions melt-rate anomaly scales with two-thirds power of the discharge. This is a stronger melt-rate dependency on discharge than found in previously studied, non-rotating cases. We also found that the melt-rate response is strongly sensitive to the location of the discharge along the grounding line; the efficiency of subglacial discharge, in terms of total melt-rate increase, grows with distance from the area where meltwater ultimately accumulates due to rotational effects (the western ice-shelf margin in this study). The relationship between melt rate and the number of sources for a given total discharge derived from non-rotating, vertical cliff experiments does not translate to the rotating ice-shelf scenario. Our results complicate the task of melt-rate parameterizations aspiring to account for subglacial discharge effects, in that there is a significant, additional melt-rate sensitivity to discharge location. The sensitivity to the location of discharge also lends new importance to accurate modeling of subglacial hydrology.

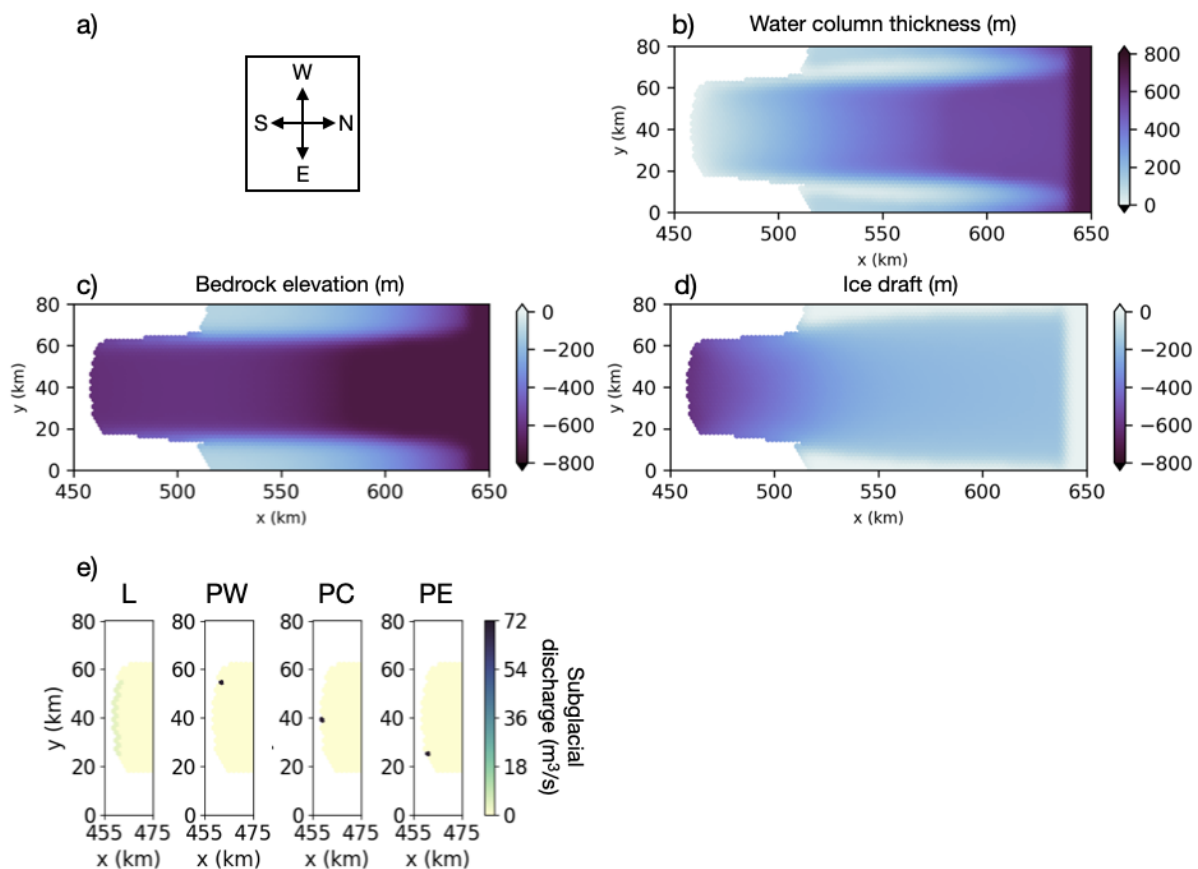


Figure 1. a) Convention for geographic references in text. b-d) Idealized ISOMIP+ domain setup. b) Water column thickness. c) Bedrock elevation. d) Ice draft. e) Distribution of subglacial discharge of $F_s = 72 \text{ m}^3/\text{s}$ at the grounding line along a line (L) or at a point west (PW), center (PC), or east (PE).

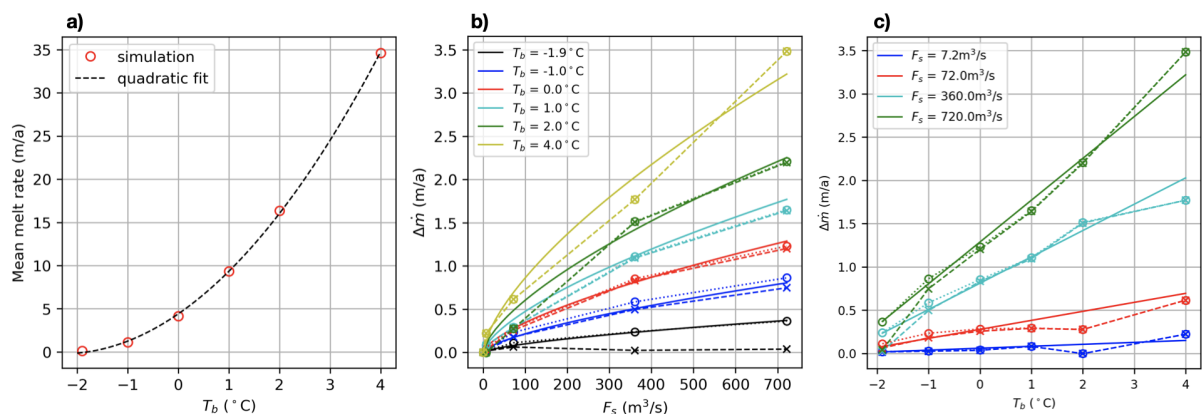


Figure 2. a) Mean reference basal melt rate for different shelf conditions set by property restoring at the northern boundary; T_b is the sea floor restoring potential temperature. The dashed line shows a quadratic fit. b) The relationship between the spatially averaged melt-rate anomaly ($\Delta\dot{m}$) and distributed subglacial discharge (F_s) for a number of different T_b values. c) The relationship between $\Delta\dot{m}$ and T_b for a number of different F_s values. In b) and c), the circles connected by dotted lines are modeled anomalies in interfacial melt rate, while the crosses connected by dashed lines are modeled anomalies in total melt rate; the sum of interfacial melt rate and freezing rate due to frazil formation. The solid line is the fit from Equation 1.

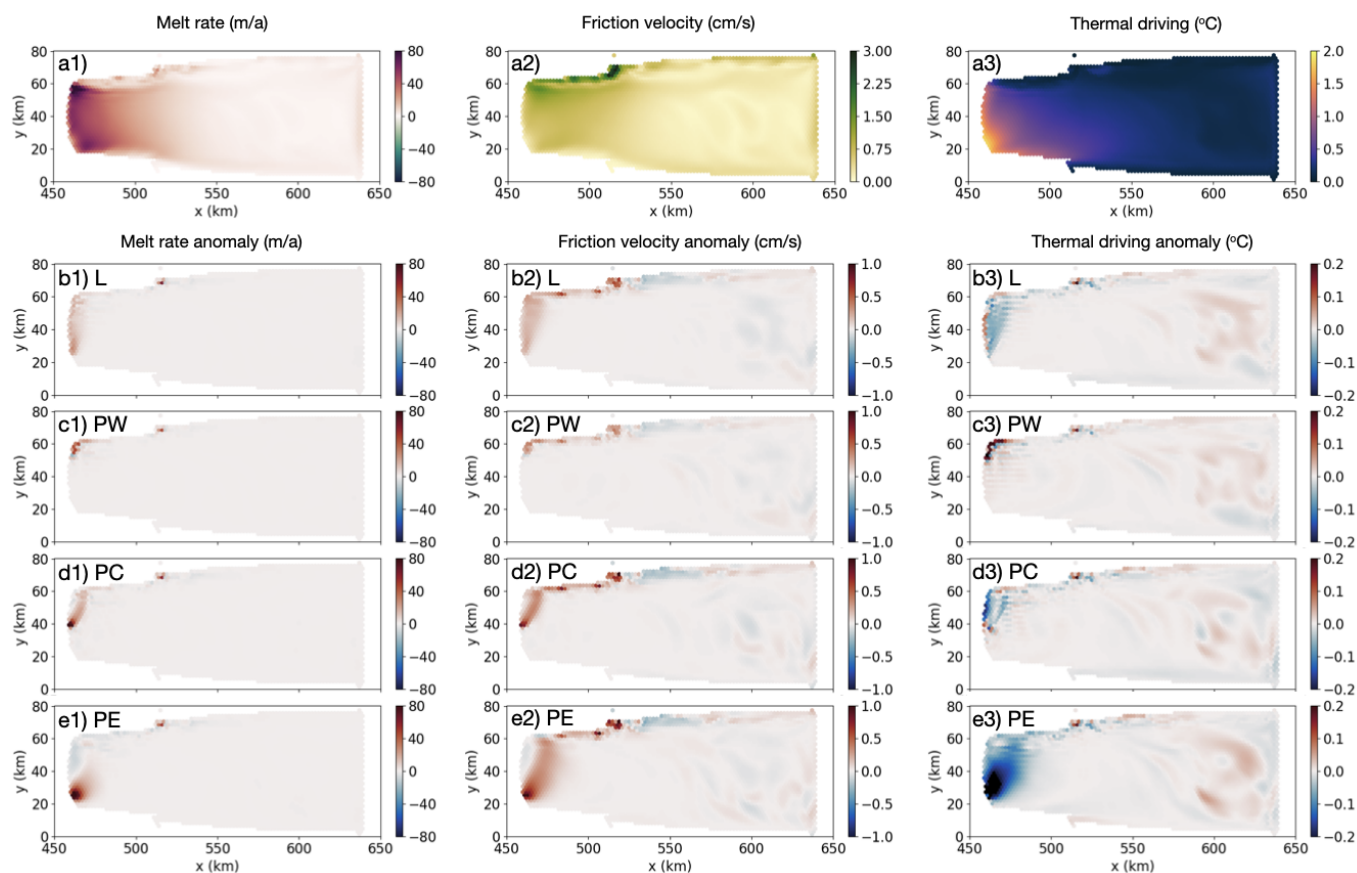


Figure 3. a) Melt rate, friction velocity, and thermal driving for the reference case without subglacial discharge ($F_s = 0 \text{ m}^3/\text{s}$). b-e) Melt-rate, friction-velocity, and thermal-driving anomalies when $F_s = 72 \text{ m}^3/\text{s}$ is added at various locations along the grounding line. b) F_s is distributed along a line (L). c-e) F_s is channelized, released at c) point west (PW), d) point center (PC), and e) point east (PE).

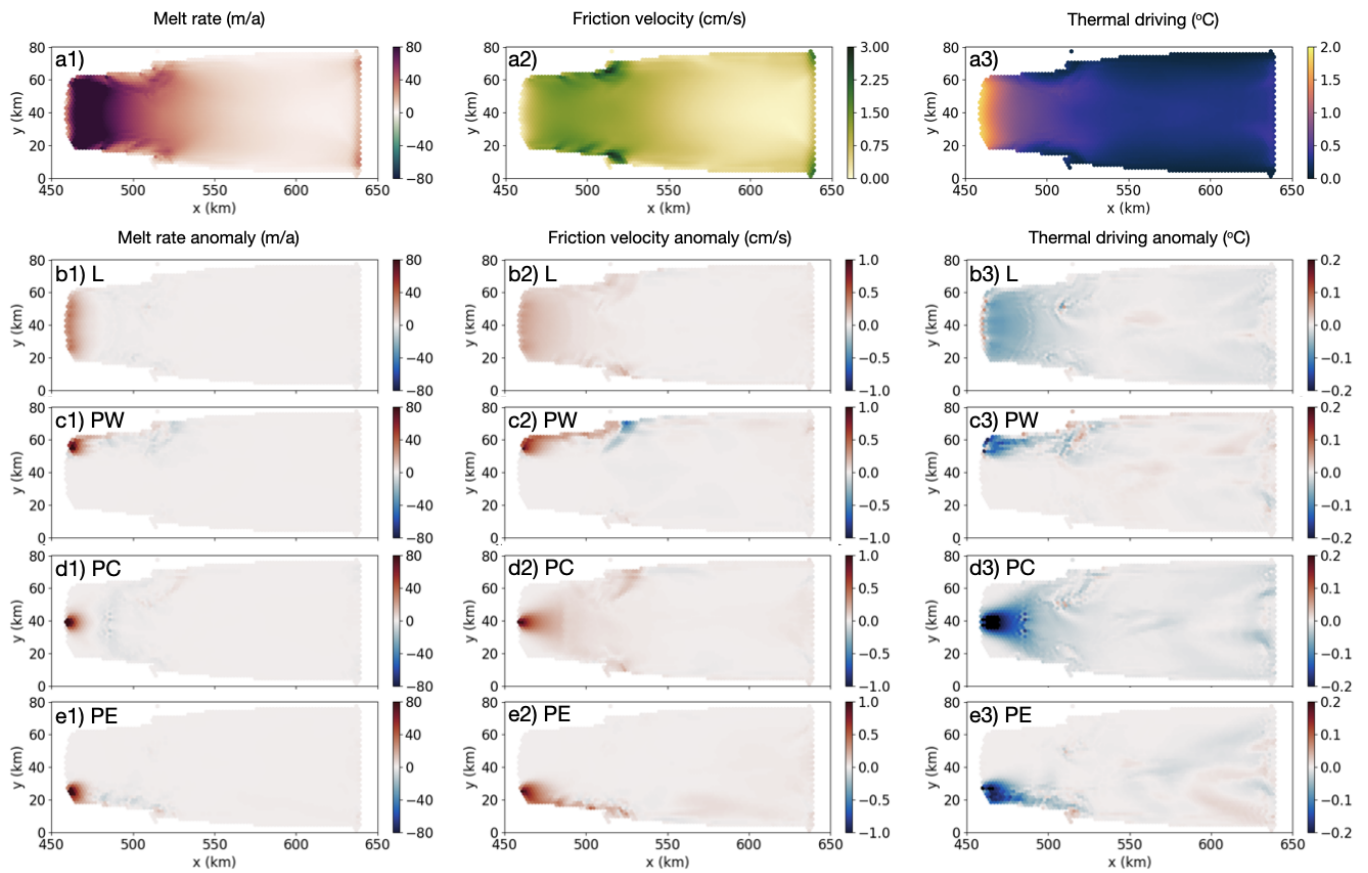


Figure 4. Same as Figure 3 but for the non-rotating case.

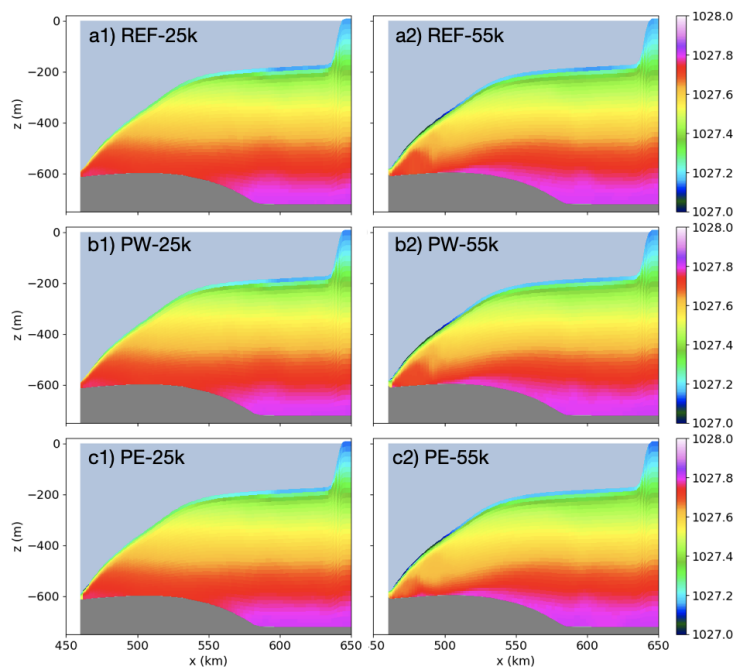


Figure 5. Potential density sections. a) Reference case without subglacial discharge ($F_s = 0 \text{ m}^3/\text{s}$). b) Channelized discharge ($F_s = 72 \text{ m}^3/\text{s}$) applied at point west (PW). c) same as b) but for point east (PE). The sections are located at $y = 25$ and 55 km , from left to right, corresponding to progression from east to west (Figure 1).

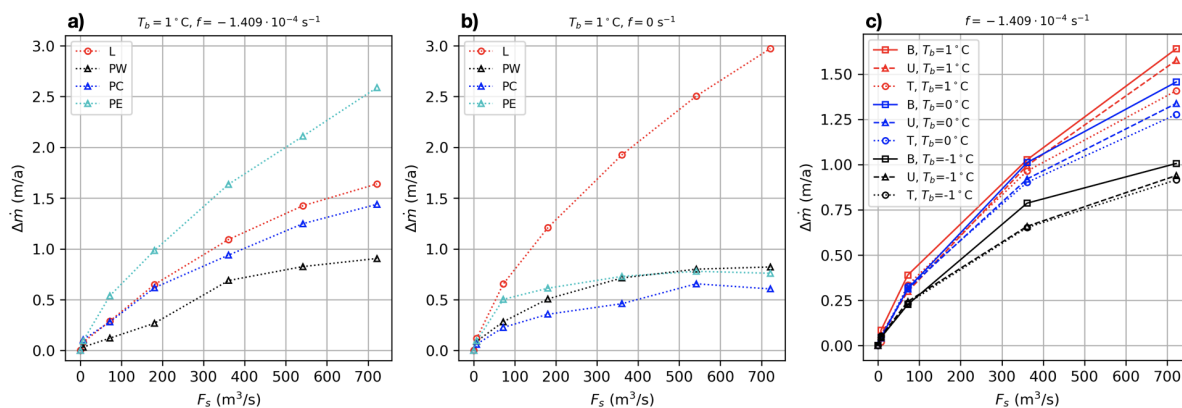


Figure 6. Spatially averaged melt-rate anomaly ($\Delta\dot{m}$) as a function of subglacial discharge (F_s) and its release location and distribution. a) Rotating case, horizontal distribution sensitivity: F_s is distributed along a line (L) or released at different channelized points (west - PW, center - PC, east - PE). b) Same as a) for the non-rotating case. c) Rotating case, sensitivity to vertical F_s release location for different temperatures: F_s is distributed along a line (L) and released at the bottom (B) layer, top (T) layer, or uniformly mixed in the vertical (U).

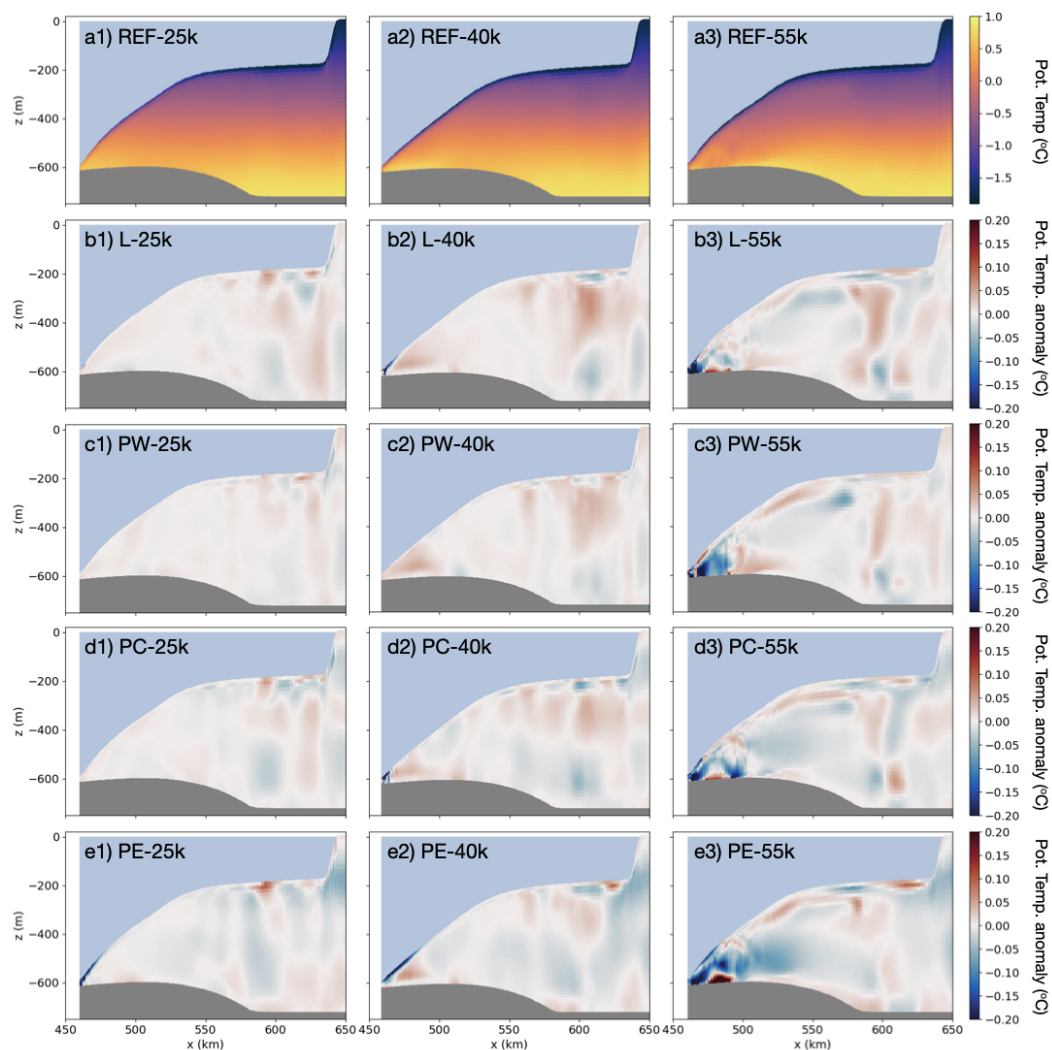


Figure 7. a) Potential temperature sections for the reference case without subglacial discharge ($F_s = 0 \text{ m}^3/\text{s}$). b-e) Potential temperatures anomalies when $F_s = 72 \text{ m}^3/\text{s}$ is added at various locations along the grounding line. b) F_s is distributed along a line (L). c-e) F_s is channelized, released at c) point west (PW), d) point center (PC), and e) point east (PE). The sections are located at $y = 25, 40,$ and 55 km , from left to right, corresponding to progression from east to west (Figure 1).

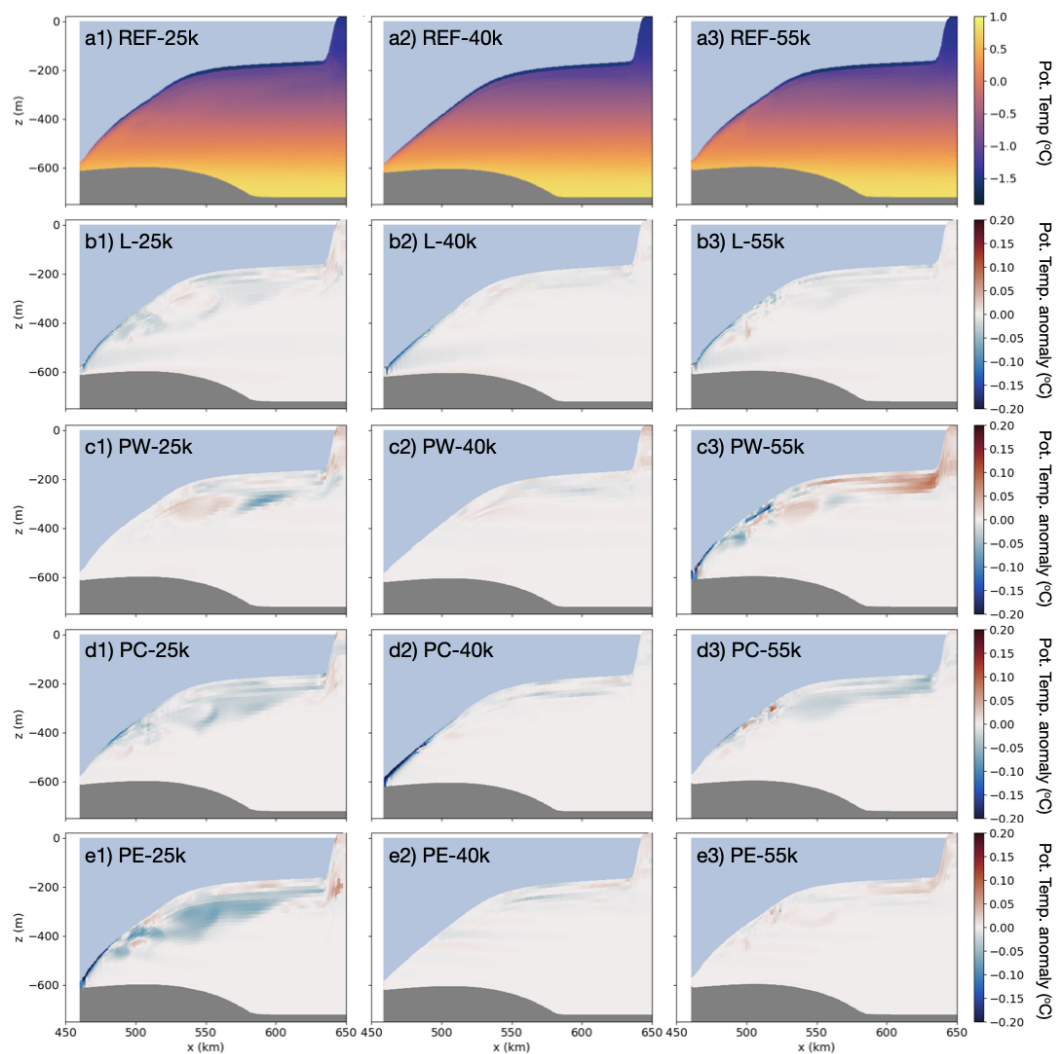


Figure 8. Same as Figure 7 but for the non-rotating case.

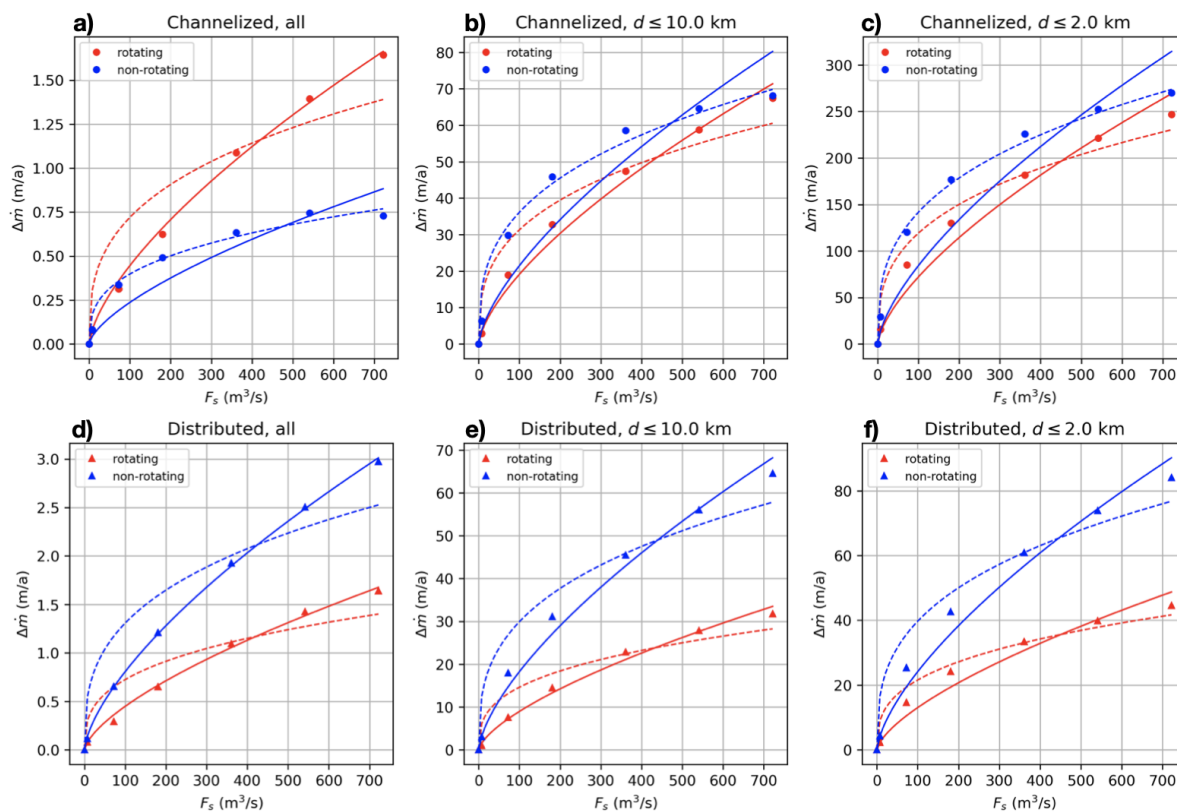


Figure 9. The relationship between spatially averaged melt-rate anomaly ($\Delta\dot{m}$) and subglacial discharge (F_s). a-c) Channelized discharge from averaged PW, PC, and PE experiments as in Figure 6a-b. d-f) Distributed discharge experiments. The melt-rate anomaly is spatially averaged over the entire ice shelf in a) and d), over a region within 10-km from the discharge location in b) and e), and over a region within 2-km from the discharge location in c) and f). The rotating case is in red, and the non-rotating case in blue. The dashed line is $\Delta\dot{m}$ scaling with F_s to one-third power and the solid line is $\Delta\dot{m}$ scaling with F_s to two-thirds power, using least squares fit.



Code availability. The E3SM code is available at <https://github.com/E3SM-Project/E3SM>, and the branch used for the simulations presented here is https://github.com/irenavankova/E3SM/tree/sg_pull_w_fraz (Git hash: 52b7bf50d52f7d9d4214ae656f225fb45223a2ee). The test cases were constructed and run using COMPASS (Configuration Of Model for Prediction Across Scales Setups), available at <https://github.com/MPAS-Dev/compass>.

Author contributions. IV conceptualized the research, coded the freshwater discharge flux feature into MPAS-Ocean and E3SM, conducted the simulations, analyzed the results, made the plots, and wrote the original manuscript. XAD and IV discussed and shaped the research along the way. XAD, DC, and JW provided software support. XAD, CBB, DC, AH, MH, and SFP contributed to the review and editing process. MH, SFP, and IV contributed funding and acquired resources.

Competing interests. The contact author has declared that none of the authors has any competing interests.

Acknowledgements. Support for this work was provided through the Scientific Discovery through Advanced Computing (SciDAC) program funded by the US Department of Energy (DOE), Office of Science, Advanced Scientific Computing Research and Biological and Environmental Research Programs. IV also received funding from the Laboratory Directed Research and Development program of Los Alamos National Laboratory under project number 20220812PRD4. This research used resources provided by the Los Alamos National Laboratory Institutional Computing Program, which is supported by the U.S. Department of Energy National Nuclear Security Administration under Contract No. 89233218CNA000001. We gratefully acknowledge the computing resources provided on Blues, a high-performance computing cluster operated by the Laboratory Computing Resource Center at Argonne National Laboratory.



References

- Adcroft, A. and Campin, J.-M.: Rescaled Height Coordinates for Accurate Representation of Free-Surface Flows in Ocean Circulation
305 Models, *Ocean Modelling*, 7, 269–284, <https://doi.org/10.1016/j.ocemod.2003.09.003>, 2004.
- Asay-Davis, X. S., Cornford, S. L., Durand, G., Galton-Fenzi, B. K., Gladstone, R. M., Gudmundsson, G. H., Hattermann, T., Holland, D. M., Holland, D., Holland, P. R., Martin, D. F., Mathiot, P., Pattyn, F., and Seroussi, H.: Experimental Design for Three Interrelated Marine Ice Sheet and Ocean Model Intercomparison Projects: MISMIP v. 3 (MISMIP +), ISOMIP v. 2 (ISOMIP +) and MISOMIP v. 1 (MISOMIP1), *Geoscientific Model Development*, 9, 2471–2497, <https://doi.org/10.5194/gmd-9-2471-2016>, 2016.
- 310 Burgard, C., Jourdain, N. C., Reese, R., Jenkins, A., and Mathiot, P.: An Assessment of Basal Melt Parameterisations for Antarctic Ice Shelves, *The Cryosphere*, 16, 4931–4975, <https://doi.org/10.5194/tc-16-4931-2022>, 2022.
- Cai, C., Rignot, E., Menemenlis, D., and Nakayama, Y.: Observations and Modeling of Ocean-Induced Melt beneath Petermann Glacier Ice Shelf in Northwestern Greenland, *Geophysical Research Letters*, 44, 8396–8403, <https://doi.org/10.1002/2017GL073711>, 2017.
- Carroll, D., Sutherland, D. A., Shroyer, E. L., Nash, J. D., Catania, G. A., and Stearns, L. A.: Subglacial Discharge-Driven Renewal of
315 Tidewater Glacier Fjords, *Journal of Geophysical Research: Oceans*, 122, 6611–6629, <https://doi.org/10.1002/2017JC012962>, 2017.
- Dow, C. F., Ross, N., Jeofry, H., Siu, K., and Siegert, M. J.: Antarctic Basal Environment Shaped by High-Pressure Flow through a Subglacial River System, *Nature Geoscience*, 15, 892–898, <https://doi.org/10.1038/s41561-022-01059-1>, 2022.
- Fürst, J. J., Durand, G., Gillet-Chaulet, F., Tavard, L., Rankl, M., Braun, M., and Gagliardini, O.: The Safety Band of Antarctic Ice Shelves, *Nature Climate Change*, 6, 479–482, <https://doi.org/10.1038/nclimate2912>, 2016.
- 320 Gagliardini, O., Durand, G., Zwinger, T., Hindmarsh, R. C. A., and Le Meur, E.: Coupling of Ice-Shelf Melting and Buttressing Is a Key Process in Ice-Sheets Dynamics, *Geophysical Research Letters*, 37, <https://doi.org/10.1029/2010GL043334>, 2010.
- Gladish, C. V., Holland, D. M., Rosing-Asvid, A., Behrens, J. W., and Boje, J.: Oceanic Boundary Conditions for Jakobshavn Glacier. Part I: Variability and Renewal of Ilulissat Icefjord Waters, 2001–14, *Journal of Physical Oceanography*, 45, 3–32, <https://doi.org/10.1175/JPO-D-14-0044.1>, 2015.
- 325 Goldberg, D. N., Twelves, A. G., Holland, P. R., and Wearing, M. G.: The Non-Local Impacts of Antarctic Subglacial Runoff, *Journal of Geophysical Research: Oceans*, 128, e2023JC019823, <https://doi.org/10.1029/2023JC019823>, e2023JC019823 2023JC019823 2023JC019823, 2023.
- Gwyther, D. E., Dow, C. F., Jendersie, S., Gourmelen, N., and Galton-Fenzi, B. K.: Subglacial Freshwater Drainage Increases Simulated Basal Melt of the Totten Ice Shelf, *Geophysical Research Letters*, 50, e2023GL103765, <https://doi.org/10.1029/2023GL103765>,
330 e2023GL103765 2023GL103765, 2023.
- Hager, A. O., Hoffman, M. J., Price, S. F., and Schroeder, D. M.: Persistent, Extensive Channelized Drainage Modeled beneath Thwaites Glacier, West Antarctica, *The Cryosphere*, 16, 3575–3599, <https://doi.org/10.5194/tc-16-3575-2022>, 2022a.
- Hager, A. O., Sutherland, D. A., Amundson, J. M., Jackson, R. H., Kienholz, C., Motyka, R. J., and Nash, J. D.: Subglacial Discharge Reflux and Buoyancy Forcing Drive Seasonality in a Silled Glacial Fjord, *Journal of Geophysical Research: Oceans*, 127, e2021JC018355, <https://doi.org/10.1029/2021JC018355>, e2021JC018355 2021JC018355
335 e2021JC018355 2021JC018355, 2022b.
- Holland, D. M. and Jenkins, A.: Modeling Thermodynamic Ice–Ocean Interactions at the Base of an Ice Shelf, *Journal of Physical Oceanography*, 29, 1787–1800, [https://doi.org/10.1175/1520-0485\(1999\)029<1787:MTIOIA>2.0.CO;2](https://doi.org/10.1175/1520-0485(1999)029<1787:MTIOIA>2.0.CO;2), 1999.



- Holland, P. R., Jenkins, A., and Holland, D. M.: The Response of Ice Shelf Basal Melting to Variations in Ocean Temperature, *Journal of Climate*, 21, 2558–2572, <https://doi.org/10.1175/2007JCLI1909.1>, 2008.
- Jackson, R. H., Motyka, R. J., Amundson, J. M., Abib, N., Sutherland, D. A., Nash, J. D., and Kienholz, C.: The Relationship Between Submarine Melt and Subglacial Discharge From Observations at a Tidewater Glacier, *Journal of Geophysical Research: Oceans*, 127, e2021JC018204, <https://doi.org/10.1029/2021JC018204>, e2021JC018204 2021JC018204 2021JC018204 2021JC018204, 2022.
- 345 Jenkins, A.: A One-Dimensional Model of Ice Shelf-Ocean Interaction, *Journal of Geophysical Research: Oceans*, 96, 20671–20677, <https://doi.org/10.1029/91JC01842>, 1991.
- Jenkins, A.: Convection-Driven Melting near the Grounding Lines of Ice Shelves and Tidewater Glaciers, *Journal of Physical Oceanography*, 41, 2279–2294, <https://doi.org/10.1175/JPO-D-11-03.1>, 2011.
- Jenkins, A., Shoosmith, D., Dutrieux, P., Jacobs, S., Kim, T. W., Lee, S. H., Ha, H. K., and Stammerjohn, S.: West Antarctic Ice Sheet Retreat
350 in the Amundsen Sea Driven by Decadal Oceanic Variability, *Nature Geoscience*, 11, 733–738, <https://doi.org/10.1038/s41561-018-0207-4>, 2018.
- Joughin, I., Shapero, D., and Dutrieux, P.: Responses of the Pine Island and Thwaites Glaciers to Melt and Sliding Parameterizations, *The Cryosphere*, 18, 2583–2601, <https://doi.org/10.5194/tc-18-2583-2024>, 2024.
- Kimura, S., Holland, P. R., Jenkins, A., and Piggott, M.: The Effect of Meltwater Plumes on the Melting of a Vertical Glacier Face, *Journal
355 of Physical Oceanography*, 44, 3099–3117, <https://doi.org/10.1175/JPO-D-13-0219.1>, 2014.
- Lazeroms, W. M. J., Jenkins, A., Gudmundsson, G. H., and van de Wal, R. S. W.: Modelling Present-Day Basal Melt Rates for Antarctic Ice Shelves Using a Parametrization of Buoyant Meltwater Plumes, *The Cryosphere*, 12, 49–70, <https://doi.org/10.5194/tc-12-49-2018>, 2018.
- Losch, M.: Modeling Ice Shelf Cavities in a z Coordinate Ocean General Circulation Model, *Journal of Geophysical Research: Oceans*, 113, <https://doi.org/10.1029/2007JC004368>, 2008.
- 360 Motyka, R. J., Hunter, L., Echelmeyer, K. A., and Connor, C.: Submarine Melting at the Terminus of a Temperate Tidewater Glacier, LeConte Glacier, Alaska, USA, *Annals of Glaciology*, 36, 57–65, 2003.
- Nakayama, Y., Cai, C., and Seroussi, H.: Impact of Subglacial Freshwater Discharge on Pine Island Ice Shelf, *Geophysical Research Letters*, 48, e2021GL093923, <https://doi.org/10.1029/2021GL093923>, e2021GL093923 2021GL093923 2021GL093923 2021GL093923, 2021.
- 365 Pelle, T., Greenbaum, J. S., Dow, C. F., Jenkins, A., and Morlighem, M.: Subglacial Discharge Accelerates Future Retreat of Denman and Scott Glaciers, East Antarctica, *Science Advances*, 9, eadi9014, <https://doi.org/10.1126/sciadv.adi9014>, 2023.
- Reese, R., Gudmundsson, G. H., Levermann, A., and Winkelmann, R.: The Far Reach of Ice-Shelf Thinning in Antarctica, *Nature Climate Change*, 8, 53, <https://doi.org/10.1038/s41558-017-0020-x>, 2018.
- Ringler, T., Petersen, M., Higdon, R. L., Jacobsen, D., Jones, P. W., and Maltrud, M.: A Multi-Resolution Approach to Global Ocean
370 Modeling, *Ocean Modelling*, 69, 211–232, <https://doi.org/10.1016/j.ocemod.2013.04.010>, 2013.
- Sciascia, R., Straneo, F., Cenedese, C., and Heimbach, P.: Seasonal Variability of Submarine Melt Rate and Circulation in an East Greenland Fjord, *Journal of Geophysical Research: Oceans*, 118, 2492–2506, <https://doi.org/10.1002/jgrc.20142>, 2013.
- Slater, D. A., Nienow, P. W., Cowton, T. R., Goldberg, D. N., and Sole, A. J.: Effect of Near-Terminus Subglacial Hydrology on Tidewater Glacier Submarine Melt Rates, *Geophysical Research Letters*, 42, 2861–2868, <https://doi.org/10.1002/2014GL062494>, 2015.



- 375 Slater, D. A., Straneo, F., Das, S. B., Richards, C. G., Wagner, T. J. W., and Nienow, P. W.: Localized Plumes Drive Front-Wide Ocean
Melting of A Greenlandic Tidewater Glacier, *Geophysical Research Letters*, 45, 12,350–12,358, <https://doi.org/10.1029/2018GL080763>,
2018.
- Slater, D. A., Felikson, D., Straneo, F., Goelzer, H., Little, C. M., Morlighem, M., Fettweis, X., and Nowicki, S.: Twenty-First Century Ocean
Forcing of the Greenland Ice Sheet for Modelling of Sea Level Contribution, *The Cryosphere*, 14, 985–1008, [https://doi.org/10.5194/tc-](https://doi.org/10.5194/tc-14-985-2020)
380 14-985-2020, 2020.
- Washam, P., Nicholls, K. W., Münchow, A., and Padman, L.: Summer Surface Melt Thins Petermann Gletscher Ice Shelf by Enhancing
Channelized Basal Melt, *Journal of Glaciology*, pp. 1–13, <https://doi.org/10.1017/jog.2019.43>, 2019.
- Wekerle, C., McPherson, R., von Appen, W.-J., Wang, Q., Timmermann, R., Scholz, P., Danilov, S., Shu, Q., and Kanzow, T.: At-
lantic Water Warming Increases Melt below Northeast Greenland’s Last Floating Ice Tongue, *Nature Communications*, 15, 1336,
385 <https://doi.org/10.1038/s41467-024-45650-z>, 2024.
- Wiskandt, J., Koszalka, I. M., and Nilsson, J.: Basal Melt Rates and Ocean Circulation under the Ryder Glacier Ice Tongue and Their
Response to Climate Warming: A High-Resolution Modelling Study, *The Cryosphere*, 17, 2755–2777, [https://doi.org/10.5194/tc-17-](https://doi.org/10.5194/tc-17-2755-2023)
2755-2023, 2023.
- Xu, Y., Rignot, E., Menemenlis, D., and Koppes, M.: Numerical Experiments on Subaqueous Melting of Greenland Tide-
water Glaciers in Response to Ocean Warming and Enhanced Subglacial Discharge, *Annals of Glaciology*, 53, 229–234,
390 <https://doi.org/10.3189/2012AoG60A139>, 2012.
- Xu, Y., Rignot, E., Fenty, I., Menemenlis, D., and Flexas, M. M.: Subaqueous Melting of Store Glacier, West Greenland from
Three-Dimensional, High-Resolution Numerical Modeling and Ocean Observations, *Geophysical Research Letters*, 40, 4648–4653,
<https://doi.org/10.1002/grl.50825>, 2013.
- 395 Zhang, T., Price, S. F., Hoffman, M. J., Perego, M., and Asay-Davis, X.: Diagnosing the Sensitivity of Grounding-Line Flux to Changes in
Sub-Ice-Shelf Melting, *The Cryosphere*, 14, 3407–3424, <https://doi.org/10.5194/tc-14-3407-2020>, 2020.